

Hybrid Lyot Coronagraph for WFIRST: High Contrast Testbed Demonstration in Flight-like Low Flux Environment

Byoung-Joon Seo^a, Fang Shi^a, Bala Balasubramanian^a, Eric Cady^a, Brian Gordon^a,
Brian Kern^a, Raymond Lam^a, David Marx^a, Dwight Moody^a, Richard Muller^a,
Keith Patterson^a, Ilya Poberezhskiy^a, Camilo Mejia Prada^a,
A. J. Eldorado Riggs^a, John Trauger^a, and Daniel Wilson^a

^a Jet Propulsion Laboratory, California Institute of Technology, Pasadena, CA. 91109

ABSTRACT

In order to validate required operation of the proposed Wide-Field InfraRed Survey Telescope (WFIRST) coronagraph instrument, we have built a testbed in Jet Propulsion Laboratory (JPL), which is analogous to the baseline WFIRST coronagraph instrument architecture. Since its birth in 2016, this testbed, named as Occulting Mask Coronagraph (OMC) testbed, has demonstrated several crucial technological milestones: Broadband high contrast demonstration in both Hybrid Lyot Coronagraph (HLC) and Shape Pupil Coronagraph (SPC) modes while the Low Order Wavefront Sensing and Control (LOWFS/C) subsystem senses and corrects the dynamic flight-like wavefront disturbances. In this paper, we present up-to-date progress of HLC mode demonstration in the OMC testbed. While injecting the flight-like low photon flux starlight with expected Line of Sight (LoS) and Wavefront Error (WFE) perturbation to the OMC testbed, we demonstrate generating high contrast dark hole images. We first study the expected photon flux in actual flight environment, and estimate detection noise and estimation accuracy of the complex electric field if the wavefront sensing algorithm is used based on the pair-wise difference imaging. Then, we introduce our improved scheme to mitigate this photon-starved flight-like low flux environment. As a result, we generate a dark hole that meets the WFIRST raw contrast requirements using the 2nd magnitude star light. We establish the key ideas, describe test setups, and demonstrate test results with data analysis.

Keywords: WFIRST, HLC, Coronagraph, Testbed, Exoplanet

1. INTRODUCTION

Wide-Field InfraRed Survey Telescope (WFIRST) is the 2.4 meter diameter telescope of National Aeronautics and Space Administration (NASA) and is the top-ranked large space mission in the New Worlds New Horizons Decadal Survey of Astronomy and Astrophysics.¹ Since the Coronagraph Instrument (CGI) was added to the WFIRST mission in 2013, our WFIRST testbed team at Jet Propulsion Laboratory (JPL) has made a couple of important milestones: Both Hybrid Lyot Coronagraph (HLC) and Shape Pupil Coronagraph (SPC) demonstrated a raw contrast below 1×10^{-8} using 10% bandwidth filter around the center wavelength of 550 nm.² The Low Order Wavefront Sensing and Control (LOWFS/C) subsystem also achieved its goal of providing sensing of Line of Sight (LoS) pointing jitter and control at 0.4 masRMS, when the WFIRST telescope provides pointing drift and jitter.³ These demonstrations are all done in three separate testbeds in JPL's High Contrast Imaging Testbed (HCIT) facility by 2015.

In order to proceed further and guide the technology development of the WFIRST CGI, we have built a new testbed in 2016. This testbed, named as "Occulting Mask Coronagraph (OMC) testbed", is designed analogous to the WFIRST flight instrument OMC architecture: It can operate in both HLC and SPC modes, and it has the LOWFS/C subsystem to sense and correct the dynamic wavefront disturbances. The OMC testbed also includes the preliminary but flight-like components such as two Deformable Mirrors (DMs), Fast Steering Mirror (FSM),

©2018 California Institute of Technology. Government sponsorship acknowledged.

The decision to implement the WFIRST mission will not be finalized until NASAs completion of the National Environmental Policy Act (NEPA) process. This document is being made available for information purposes only.

focal plane masks and lyot stop masks for both HLC and SPC modes. In addition, the OMC testbed is equipped with the dynamic Optical Telescope Assembly Simulator (OTA-S) that feeds the simulated dynamical Optical Telescope Assembly (OTA) output light (or CGI input light) enabling us to perform the WFIRST dynamic test. Using the OMC testbed, we have previously demonstrated both generating and maintaining the dark holes in the flight-like LoS and Wavefront Error (WFE) perturbation environment.^{4,5}

In this paper, we study another one of the most concerning effects in flight: The flight-like low photon flux. In the previous demonstrations until 2017, the photon flux has not been a control parameter in the OMC testbed. The laser power and the exposure time were set such that we obtained a sufficient Signal-to-noise ratio (SNR) for the obtained images. However, the WFIRST project requires the reference star to be magnitude of 2 or lower and the target star to be magnitude of 5 or lower. The reference star is used for making a dark hole while the target star is used for the science observation.

The remainder of this paper is structured as follows. First, in Sec. 2, we estimate the photon flux for the WFIRST CGI for various star magnitudes and compare the flight photon flux to that of the testbed star. In such a low photon flux condition as will be shown in Sec. 2, one of the most concerning problems is the potential poor accuracy in estimating the complex electric field in the dark hole. We review our complex electric field estimation process in Sec. 3 and discuss the improvement we have made to mitigate such a low photon flux condition. In Sec. 4, we describe the testbed setups and results to demonstrate generating high contrast dark hole images, which meet the WFIRST raw contrast requirement while injecting the 2nd magnitude photon flux starlight with expected LoS and WFE perturbation to the OMC testbed. After generating the dark hole with the 2nd magnitude star, we also demonstrate maintaining the dark hole with a 5th magnitude star by the LOWFS/C in a separate report.⁶ We conclude in Sec. 5 listing our future work.

2. FLIGHT FLUX ESTIMATION

In order to estimate the photon flux when the WFIRST CGI is operational in orbit, we first obtained the star photon flux measurement for the G0V type 0th magnitude star as shown in Fig. 1(a). We obtain Fig. 1(a) based on the A0V type 0th magnitude UBVRI data and the color correction given in [7]. We also verify this star photon flux measurement of the G0V type star by comparing it to an independent star photon flux measurement from a previous JPL project.

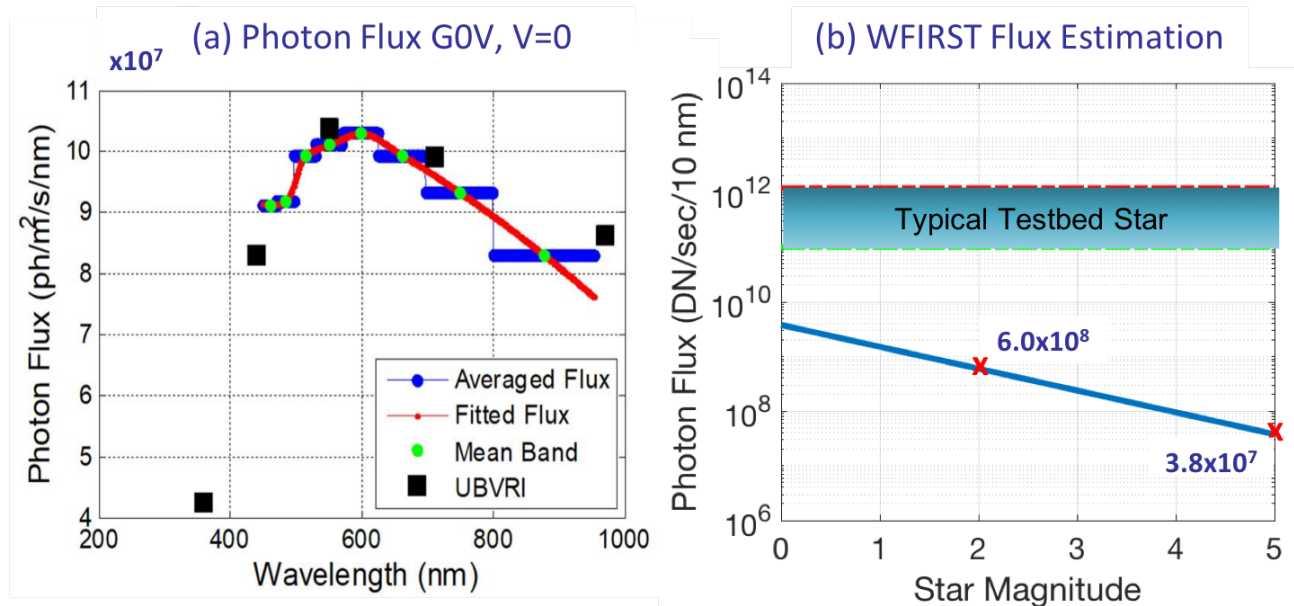


Figure 1. Photon Flux Estimation. (a) Star photon flux estimation for the G0V type 0th magnitude star, which is based on data from [7]. (b) Estimation of the total DN flux that can be imaged on the WFIRST CGI detector with 10 nm spectral bandwidth at 550 nm for different star magnitudes.

Then, we estimate the total DN counts that can be imaged on the WFIRST CGI detector as shown in Fig. 1(b). When we convert the star photon flux measurements in Fig. 1(a) to the total DN count in Fig. 1(b), we assume that the star is G0V type, the center wavelength is 550 nm with bandwidth of 10 nm, total propagation loss is 0.566×0.9 , the detector Quantum Efficiency (QE) is 0.929, and the electron-to-DN conversion ratio is 2. The total propagation loss is the Current Best Estimation (CBE) including total reflection loss of 0.566 for all the mirror surfaces in both the WFIRST observatory and the CGI, and the transmission estimation of 0.9 for the wavelength selecting color filter. The detector QE is also the CBE of the WFIRST CGI science camera at the operation wavelength of 575 nm. We ignore the difference between the testbed operating wavelength of 550 nm and the WFIRST science wavelength of 575 nm for the HLC mode.

As pointed out in Sec. 1, the WFIRST project requires the reference star to be magnitude of 2 or lower and the target star to be magnitude of 5 or lower. The reference star is used for making a dark hole while the target star is used for the science observation. Fig. 1(b) shows the estimated G0V type star photon flux is 6×10^8 DN/sec/10nm and 3.8×10^7 DN/sec/10nm for the 2nd and 5th magnitude stars, respectively. These values are compared to the typical testbed star photon flux ranging from 1.2×10^{11} DN/sec/10nm to 1.0×10^{12} DN/sec/10nm, which is 200 or 2000 times brighter than the 2nd magnitude star. For the testbed photon flux measurement, we use the pupil images rather than the focal images with no coronagraphic elements in the optical path such as the focal plane mask, the field stop mask and the lyot stop mask. We also ignore the throughput difference between the focusing lens and the pupil lens in the OMC testbed.

We vary the star brightness in the testbed by adjusting the laser source power. By reducing the laser source power sufficiently enough, we can match the testbed star brightness to that of the reference 2nd magnitude star. If we do, our testbed operation time would be same as the flight operation time. Then, our test cycle becomes unnecessarily long. Furthermore, we may need to fight unnecessarily with the testbed drift, which is most likely different from the actual drift in flight. Therefore, throughout this paper, we operate the testbed with the star flux of 1.2×10^{11} DN/sec/10nm, which is 200 times brighter than the 2nd magnitude star. In order to match the photon or DN counts, we reduce the exposure time by 200 times instead. This means that the testbed operation time is 200 times faster than the flight operation time: The single image exposure time of the testbed, t_{TB} , is 200 times smaller than the flight-equivalent single image exposure time, t_{flight} . For example, 0.4 sec of t_{TB} is equivalent to 80 sec of t_{flight} , which is our baseline test setup for the low flux test described in Sec. 4.

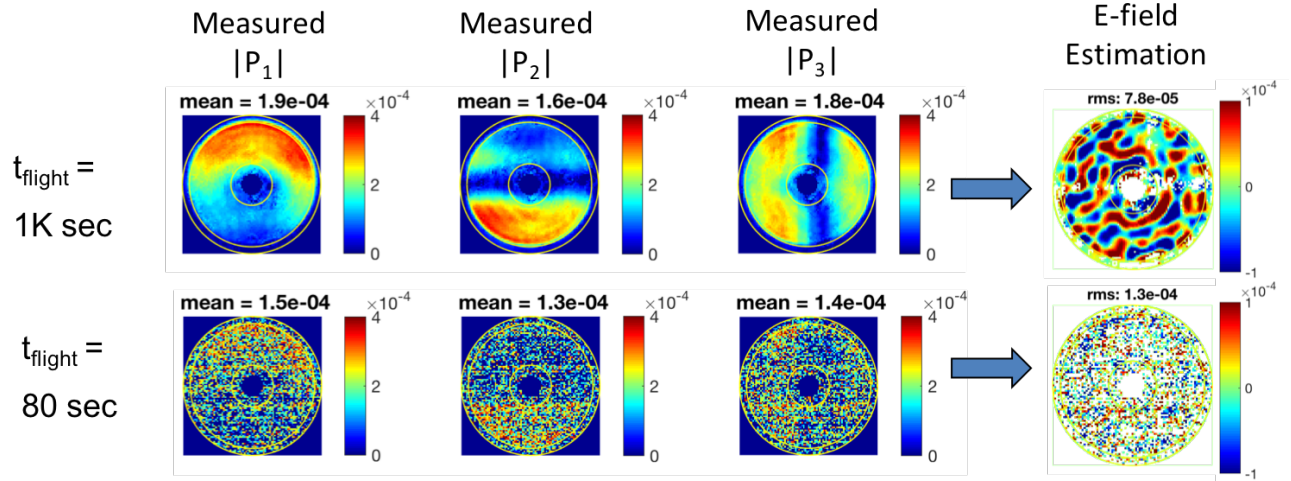


Figure 2. The measured probe amplitudes, $|P_j|$, in Eq. (1) and estimated complex electric field (only the real part is shown here for simplicity.) with different single image exposure time. The top row is obtained with t_{TB} of 5 second or t_{flight} of 1×10^3 sec. The bottom row is the same as the top row except we use t_{TB} of 0.4 second or t_{flight} of 80 sec.

3. MEASUREMENT NOISE IN COMPLEX ELECTRIC FIELD ESTIMATION

As predicted in Sec. 2, a photon-starved condition is expected when the WFIRST CGI is operational in orbit. One of the most critical problems in this photon-starved condition is the potential poor accuracy in estimating complex electric field.

In measuring the complex electric fields in the dark hole region, we employ the pairwise estimation scheme.^{8,9} In this method, “probes”⁸ are placed on one of the DMs (DM1 for our case) to modulate the complex electric field across the dark hole. The probes are applied typically in pairs, providing the largest phase diversity and probe simplicity as well as minimizing DM gain uncertainty impact. Given images corresponding to several probe pairs, along with an image with no probes applied at all, we can retrieve the complex electric field at the region of interest. Our specific probing schemes and Electric Field Conjugation (EFC) implementation are detailed in our previous reports.^{4,9}

The top row in Fig. 2 shows the measured probe amplitudes, $|P_j|$, and estimated complex electric field (only the real part is shown here for simplicity.) with t_{TB} of 5 second or t_{flight} of 1×10^3 sec. The probe amplitude is defined as,

$$|P_j| = \sqrt{\frac{I_j^+ + I_j^-}{2} - I_o} \quad (1)$$

where I_j^\pm is the normalized intensity of the \pm probes made for the j 'th pair and I_o is the unprobed normalized intensity. The white circles are drawn representing 3, 9, and 10 λ/D radii in the dark hole. Note that these probe intensities, I_j^\pm , are generated using DM1 and are much larger (at least factor of 10) than the unprobed normalized intensity, I_o . On the other hand, the bottom row in Fig. 2 shows the same plots except the single image exposure time is reduced to t_{TB} of 0.4 sec or t_{flight} of 80 sec while the DM1 probe pattern and strength remain the same. With t_{flight} of 80 sec, the mean DN of the probe intensities is about 0.5 DN resulting that the probe amplitudes and the estimated complex electric field become noisy as shown in the bottom row of Fig. 2.

Our first attempt to getting a dark hole with t_{flight} of 80 sec was not very successful due to this noisy measurement. The major reason why the estimation was poor was that the probe amplitudes in Eq. (1) become pure imaginary at most pixels in the dark hole due to the noise (thus, leading to an ill-conditioned pseudo-inverse of the observation matrix in Eq. (4) in App. A).

One scheme to overcome this noisy measurement is the “probe amplitude Look-Up-Table (LUT) scheme” (or LUT scheme for short). In this scheme, the probe amplitudes, $|P_k|$, are saved as a LUT with a sufficiently large exposure time. Then, these saved probe amplitudes are reused for the photon-starved condition. Note that the probe amplitudes are independent of the existing electric field, E_o , in the dark hole if the probe amplitudes are sufficiently larger than $|E_o|$. This means that the probe amplitudes in the top and bottom rows in Fig. 2 are supposed to be same if no noise is assumed.

Fig. 3(c) shows the complex electric field estimation (real part only for simplicity) when the probe amplitudes LUT scheme is used. For comparison, other electric field measurements are also shown in Fig. 3 when (a) the high flux measurement (t_{flight} of 1×10^3 sec) and (b) low flux measurement (t_{flight} of 80 sec) with no LUT scheme. We compare the complex electric estimations without or with the probe amplitude LUT scheme in Fig. 3(b) and Fig. 3(c), and we find that most pixels now become valid with the LUT scheme.

In order to understand further how our wavefront control algorithm, EFC, interprets the measured electric field in the noisy environment, we decompose those electric fields in Fig. 3 into the SVD spectra as shown Fig. 4. The SVD spectrum of a given electric field is the linear SVD decomposition using the linear control matrix*. Our EFC decomposes the measured electric field in the SVD mode, and then regularizes the modes with a weighting function such as the “Tikhonov window”. We refer to our previous paper⁴ for detail of the SVD spectrum and our regularization in the HLC mode.

The black curve in Fig. 4 is the SVD spectrum with the high flux case of Fig. 3(a). Assuming the high flux case (black curve) is the truth, we compare it to the blue, red, and green curves in Fig. 4 for those low flux cases of Fig. 3(b,c,d). Then, we make the following interesting observation. First, we find that the probe amplitude

*Many call it the “Jacobian”

LUT scheme plays the important role by recovering the SVD spectrum: The red curve resembles better the black curve than the blue curve does. Second, the salt-and-pepper-like noise observed in the low flux with the LUT in Fig. 3(c) is mostly beyond our control region: the red curve is different from the black curve mostly in $(S/S_1)^2 < 10^{-5}$, where S is the SVD value of the mode, and S_1 is the SVD value of the fundamental mode. In EFC, our practical choice for the regularization parameter β is around -5 , meaning that only SVD modes with $(S/S_1)^2 > 10^{-5}$ are controllable as highlighted in Fig. 4. On the other hand, we have a reasonable match between the black and the red curves in the controllable region. Third, the use of the spatial filter such as Wiener filter is not helping much in the SVD spectrum space. The spatial filters are beneficial simply for visualization removing high order noises. But similar curves between the red and green curves suggests that the EFC already knows what to correct. A spatial filter is not necessary for better wavefront control. Therefore, it is our baseline control strategy not to use any numerical spacial filter.

In order to quantify the accuracy of the complex electric field measurement, Fig. 5(a) plots the “electric field measurement uncertainty” as a function of the flight-equivalent single image exposure time t_{flight} . Eq. (2)

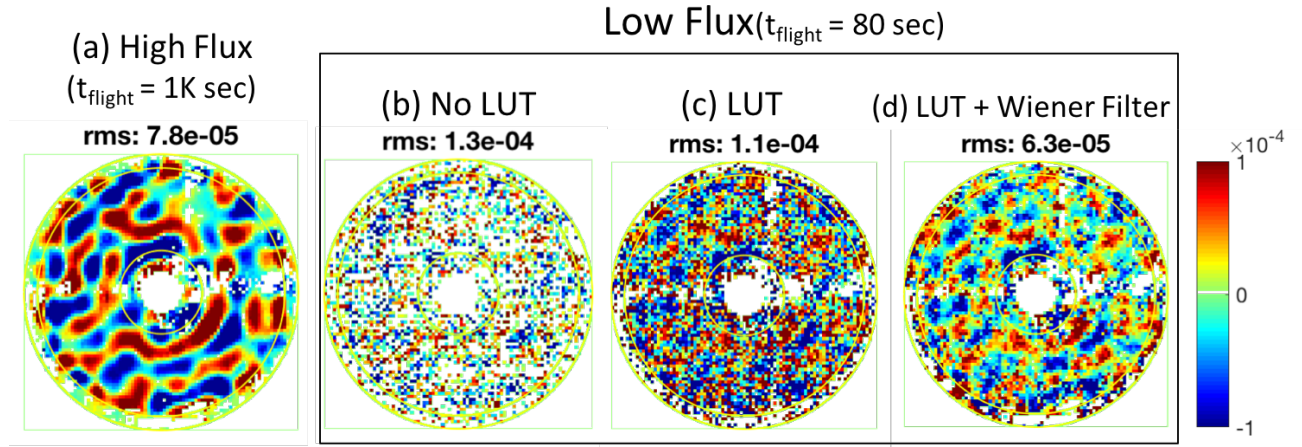


Figure 3. The complex electric field estimation at (a) high (t_{flight} of 1×10^3 sec) and (b,c,d) low (t_{flight} of 80 sec) photon flux. For the low flux measurement in (b,c,d), three different methods are used. (a) and (b) are without or with the probe amplitude LUT scheme. (c) is a Wiener filter is applied to (b).

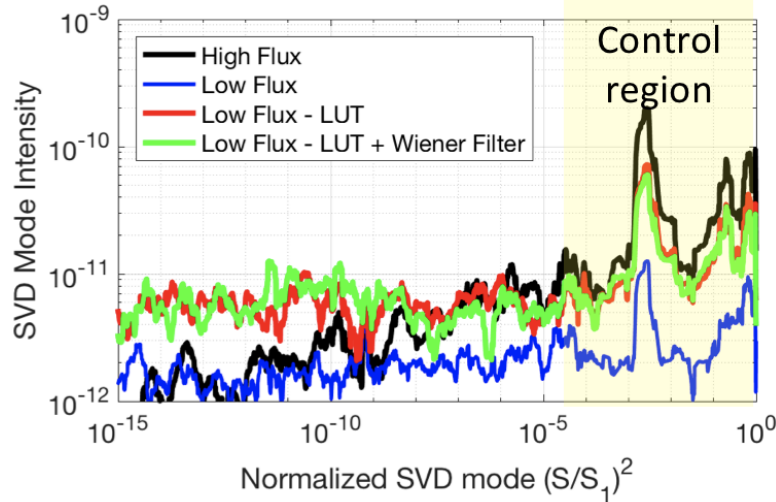


Figure 4. The SVD mode spectra for the complex electric field measurements in Fig. 3. The black curve is the SVD spectrum with the high flux case of Fig. 3(a). The blue, red and green curves are for those low flux cases of Fig. 3(b,c,d). The procedure to obtain the SVD spectra is described in [4].

formulates our definition of the electric field measurement uncertainty.

$$\sigma^2 = \langle \sigma^2(E_R) + \sigma^2(E_I) \rangle, \quad (2)$$

where σ^2 represents the variance, $\langle \cdot \rangle$ denotes the spatial average in the dark hole ($3-9 \lambda/D$), and E_R and E_I are the real and imaginary part of the complex electric field measurement.

To measure the electric field measurement uncertainty marked as “o” in Fig. 5(a), we first obtain a dark hole using EFC.^{4,9} Then, we stop EFC and measure the complex electric field in the dark hole with various t_{flight} , ranging from 1×10^4 sec down to 6 sec. For each exposure time, 4 repeated measurements are done to find the variance of real and imaginary part of the complex electric field measurement at each pixel. The data marked as “o” in Fig. 5(a) shows the variance of those 4 repeated measurements. Eq. (2) implies that we capture the electric measurement repeatability for the electric measurement uncertainty.

By stopping EFC, we stop updating DMs and we apply a fixed voltage patterns on DM1 only for probing purpose while DM2 is unchanged. For complex electric field measurement, we have three pairs of probes and consider three different wavelength, 10 nm bandwidth each centered at 530, 550, and 570 nm. Therefore, total number of probed images are 18 ($=3 \times 3 \times 2$). Three different colors in Fig. 5(a) are for different wavelengths of 530, 550 and 570 nm.

The measured data, marked with “o”, are compared to their expected uncertainties. One expected uncertainty, marked as “x”, is based on the variance of the measured probe intensity and the probing equation as

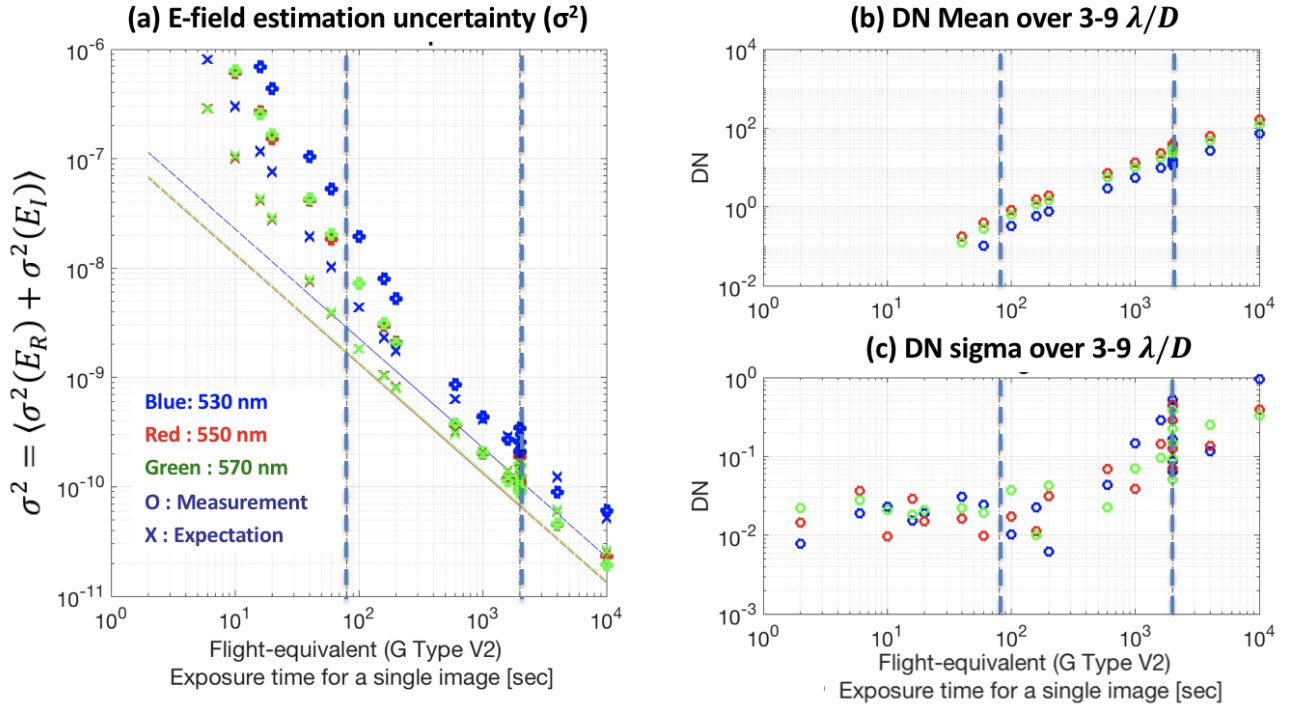


Figure 5. (a) Complex electric field estimation uncertainty defined in Eq. (2) as a function of the flight-equivalent single image exposure time t_{flight} . The measurement, marked as “o”, is based on the repeatability of the measurement. One expected uncertainty, marked as “x”, is based on the variance of the measured probe intensity and the probing equation as mathematically derived in App. A. The other expected uncertainty, marked as solid line, is what Groff, et. al.¹⁰ called as “Noise equivalent contrast”, which can be obtained assuming that the equal probe amplitude for all 6 unprobed images and that the poisson noise is dominant. (b) and (c) are the measured DN mean and standard deviation of the probe intensities, I_k^\pm . The read noise is dominant in the testbed at our low flux operating single image exposure time t_{flight} of 80sec later used in Sec. 4. Since we expect that the actual flight science camera will have better noise performance at this photon flux, our low flux test is more conservative than the actual flight in terms of the science camera capability.

mathematically derived in App. A. The other expected uncertainty, marked as solid line, is what Groff, et. al.¹⁰ called as “Noise equivalent contrast”, which can be obtained assuming that the equal probe amplitude for all 6 unprobed images and that the poisson noise is dominant.

As shown in Fig. 5(a), the measured data is well compared to those expected data as the exposure time is larger. However, we observe the slope break of the measured data at around t_{flight} of 200 sec, which implies that other noises become stronger relative to the poisson noise such as read noise and dark current noise. While a study is in progress for improving the science camera capability for the WFIRST project,¹¹ our testbed still employs a commercial camera (Neo 5.5 sCMOS, ANDOR Tech. Ltd, <http://www.andor.com/scientific-cameras/neo-and-zyla-scmos-cameras/neo-55-scmos>). According to its specification, it has less than $1 e^-$ read noise and sufficiently small dark current noise. This agrees with the measured mean DN of approximately 1 DN, as shown in Fig. 5(b) at the slope break t_{flight} of 200 sec.

Therefore, the read noise is dominant in the testbed at our low flux operating condition with the single image exposure time t_{flight} of 80 sec described later in Sec. 4. Since we expect that the actual flight science camera will have better noise performance at this photon flux, our low flux test is more conservative than the actual flight in terms of the science camera capability. However, other in-orbit noise sources, such as cosmic rays,¹¹ are not yet considered in the testbed.

4. TESTBED TEST RESULT

Fig. 6 highlights our testbed setup to demonstrate the flight-like low photon flux dynamic operation using the OMC testbed. First, we adjust the star brightness to 200 times brighter than the 2nd magnitude star as discussed earlier in Sec. 2. We configure the testbed star to have the bandwidth of 100 nm (18 %) at the center wavelength of 550 nm. Then, we have applied the flight-like perturbation of the WFIRST using the OTA-S. The

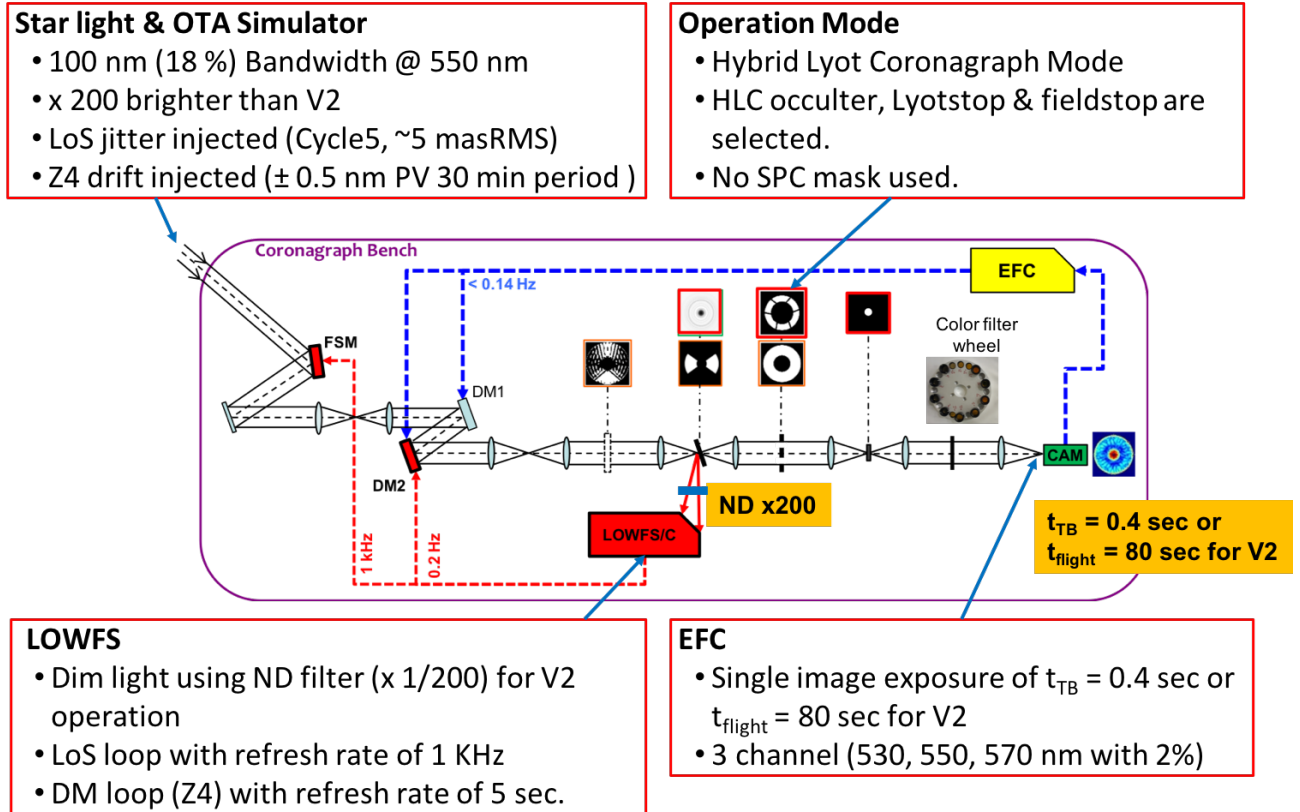


Figure 6. Test setup to demonstrate the flight-like low photon flux dynamic operation using the OMC testbed.

considered perturbation, “Cycle 5”, consists of approximately 5 mas/axis LoS jitter and 14 mas/axis LoS drift. The Cycle 5 perturbation are described in detail in [5]. This simulated LoS jitter and drift are generated by the Jitter Mirror (JM) in the OTA-S. We currently consider the defocus mode perturbation only for the WFE drift because of the limitation of the current OTA-S. We apply a sinusoidal defocus of ± 0.5 nm by moving the pinhole assembly stage back and forth along the optical axis with a period of half hour. Note that 0.5 nm is 50 times larger than the Cycle 5 WFE drift estimation of 10 pm. With these perturbations turned on, [5] demonstrates the contrast in both SPC and HLC degrades worse than $1\text{E-}7$.

To demonstrate that the LOWFS/C functions with the 2nd magnitude star, we first dim the star light using Neutral Density (ND) filter by 200 times for the LOWFS/C. The ND filter is located at the reflected path of the light between the LOWFS/C subsystem and the HLC focal plane mask (or occulter). We then turned on the LOWFS/C to cancel the perturbation. Using the equivalent 2nd magnitude star’s reflected light from the occulter, LOWFS/C senses the LoS errors and Noll Zernike modes¹² from Z4 (defocus mode) to Z11 (spherical mode).[†] Then, the LOWFS/C controls the FSM to cancel the LoS perturbation and command the DM2 to cancel the WFE. These control loops are schematically represented in Fig. 6. We refer [5,6] for the detail of the LOWFS/C.

To demonstrate that the EFC functions with the 2nd magnitude star, we fix the testbed single image exposure time t_{TB} at 0.4 sec, which is equivalent to t_{flight} of 80 sec. For the EFC, we sense and control the 3 spectral bands centered at 530 nm, 550 nm and 570 nm. Each band has 10 nm bandwidth, respectively.

There are several configuration differences between WFIRST flight and current testbed. First, the star spectrum is different. While the WFIRST will see mostly G type stars which has a somewhat flat spectrum around 575 nm as in Fig. 1(a), our testbed star spectrum is somewhat arbitrary including the laser spectrum, the pinhole throughput, and the gold-coated DM mirror reflection. Second, the EFC center wavelengths of 550 nm and bandwidth of 10 nm are different from the WFIRST HLC baseline of the center wavelength of 575 nm and the engineering filter bandwidth of 3.3%. Third, only LoS and Z4 (defocus mode) are controlled by the LOWFS/C in the testbed while the WFIRST requires the correction up to Z11 (spherical mode). Fourth, Z4 (defocus mode) is controlled by the DM2 in the testbed, while the WFIRST has a plan to control it using a focus adjusting mirror. Fifth, a commercial camera (see Sec. 3) is used in the testbed while the WFIRST will employ superior Electron-multiplying CCD (EMCCD) in the photon counting mode.¹¹

These differences are mostly because of current testbed hardware limitations. Although we have a plan to update the testbed to match better to the WFIRST flight, these differences are not dominating factors for the contrast performance except the science camera. Therefore, as we discussed in Sec. 3, our study is a conservative estimation.

Note that DM2 is controlled by both the EFC loop and the LOWFS/C loop. While the EFC requires the change of DM2 voltages to improve the dark hole, the LOWFS/C adjusts DM2 to cancel any Z4 drift in our test setup. The EFC may require low order Zernike change (Z4 in the testbed) on DM2 as well. However, this DM2 voltage change from the EFC should not be canceled by the LOWFS/C. In order to avoid this potential cancelation of Z4, we design such that the EFC shares the pre-computed Z4 reference with the LOWFS/C. That is, the LOWFS/C distinguishes the EFC-induced Z4 from the environmental Z4 drift, and only corrects the environmental Z4 drift. In flight, Z4 is controlled by the focus adjusting mirror and other higher order Zernikes (Z5-Z11) are controlled by one of the two DMs.

While the testbed is configured as described above, Fig. 7 shows the measured contrast as a function of EFC iteration. All contrast values in Fig. 7 are the 3 spectral bands’ average. Initially at the 0th iteration, we start the EFC using a previously generated DM solution, which generated a $1\text{E-}7$ contrast dark hole.

The solid blue curve in Fig. 7 indicates the measured “modulated” light. In addition to the complex electric field of the residual starlight in the dark hole, our pairwise estimation algorithm^{8,9} also can find a portion of light that does not interact with the applied probes. We refer to this light as “unmodulated” light. As the counterpart to the unmodulated light, we refer to the complex electric field of the residual starlight that responds to the probes as the “modulated” light. We refer [9] for definitions of “unmodulated” and “modulated” lights in more detail. We consider the full 360 degrees region between $3 \lambda/D$ and $9 \lambda/D$ at 550 nm for the plots in Fig. 7.

[†]Throughout this paper, “Zx” represents the Noll Zernike mode x.

Both modulated and unmodulated light measurement become noisy if the exposure time reduced. At the t_{TB} of 0.4sec, the modulated light is dominated by the noise, which is around $2\text{E-}8$ as indicated in Fig. 5. The modulated light floor of 2×10^{-8} is also observed in Fig. 7 as the iteration increases. Therefore, evaluation of both modulated and unmodulated lights is invalid with t_{TB} of 0.4sec and the contrast is better than 2×10^{-8} . For their correct evaluation, we insert an “observing iteration” every 5 iterations. At the observing iteration, we freeze the DMs and increase the exposure time. Any evaluation made at this observing iteration is excluded from the EFC. The observing iteration is only for the correct evaluation of the contrast. The green, blue, and red dots in Fig. 7 indicate the total, modulated, and unmodulated contrasts, respectively, at those observing iterations, and they are the only correct evaluation of the contrasts.

The required total iteration number to get the final dark hole is 122 as shown in Fig. 7. This is the sum

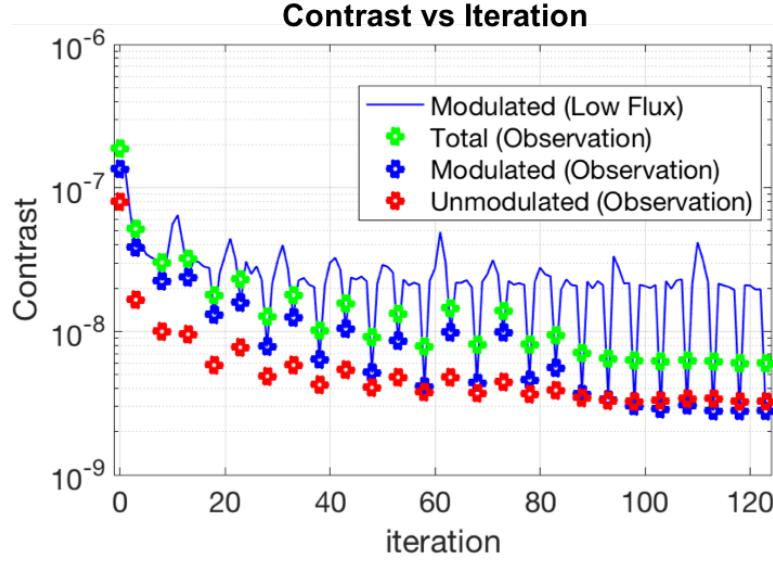


Figure 7. The measured contrast as a function of EFC iteration with the t_{TB} of 0.4sec or t_{flight} of 80sec. All contrast values are the 3 spectral bands’ average. The solid blue curve indicates the measured “modulated” light, which is dominated by the noise if the contrast is below 2×10^{-8} and the t_{TB} is 0.4sec. For their correct evaluation, we insert the “observing iteration” every 5 iterations. The green, blue, and red dots in Fig. 7 indicate the total, modulated, and unmodulated contrasts, respectively, at those observing iterations, and they are only correct evaluation of the contrasts.

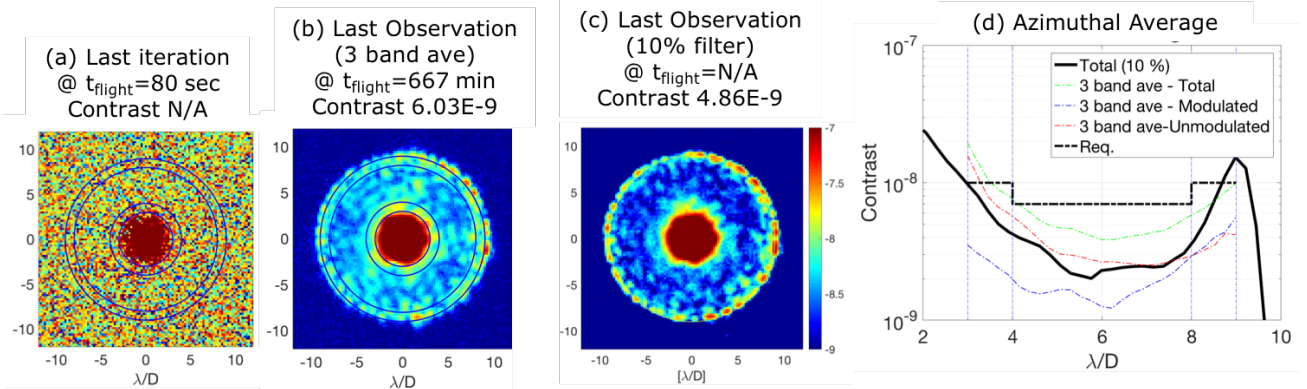


Figure 8. The contrast measured at the last iteration: (a) 3 bands’ average with t_{flight} of 80 sec, (b) 3 bands’ average with t_{flight} of 334 minutes, 667 minutes, and 667 minutes for 3 bands, respectively, (c) a single 10 % bandwidth measurement. Four blue circles in (a), (b), and (c) are drawn to represent the 3,4,8, and 9 λ/D radius field of view. (d) The azimuthal average of (b) and (c) is compared to and compares the WFIRST raw contrast requirement of 1×10^{-8} , 7×10^{-9} , and 1×10^{-8} for spatial bands of 3-4 λ/D , 4-8 λ/D , and 8-9 λ/D , respectively. (d) shows that the final 10 % average contrast (black solid curve) meets the WFIRST raw contrast requirement (black dashed lines).

of the 96 actual low flux iterations and the 26 observing iterations. If we only consider the 96 actual low flux iterations, the total exposure time sum for all images is 13.44 minutes of the testbed time, which is equivalent to 44.8 hours of the flight time. This total iteration time is not optimized yet. An optimal control strategy needs to be investigated further to improve this total iteration time. Aggressive and non-aggressive regularizations are alternated before the 80th iteration, resulting intermittent contrast degradation. See [4] for the benefit of alternating regularization.

As a result, the contrast improves at the observing iterations as the iteration increases. Fig. 8(a) shows the contrast measured at the last iteration with t_{flight} of 80 sec, which is somewhat meaningless because it is dominated by the (read) noise. Fig. 8(b) is the same contrast measurement as Fig. 8(a) but with increased exposure time t_{flight} of 334 minutes, 667 minutes, and 667 minutes for 3 bands, respectively. Fig. 8a and Fig. 8(b) are the 3 bands contrast average while Fig. 8(c) is a single 10 % bandwidth measurement. Since the contrast typically depends on the wavelength quadratically and the 3 bands samples the center and edge wavelengths, the 10 % single contrast of Fig. 8(c) is normally better than the 3 bands' averaged contrast of Fig. 8(d).

Four blue circles in Fig. 8(a), (b), and (c) are drawn to represent the 3,4,8, and 9 λ/D radius field of view. Fig. 8(d) plots the azimuthal average of Fig. 8(b) and Fig. 8(c) and compares them to the WFIRST raw contrast requirement of 1×10^{-8} , 7×10^{-9} , and 1×10^{-8} for spatial bands of 3-4 λ/D , 4-8 λ/D , and 8-9 λ/D , respectively. Fig. 8(d) shows that the final 10 % average contrast (black solid curve) meets the WFIRST raw contrast requirement (black dashed lines).

5. CONCLUSION AND FUTURE WORK

During our early testbed operation between 2013 and 2017, our focus was to validate key components and concepts for the WFIRST CGI such as the WFIRST mask, two DM operation, two HLC and SPC mode operation, the LOWFS/C operation, the electric field measurement, and so forth.

As the technology becomes mature, we are now aiming at operating the testbed in more and more flight-like environment. Our goal is first to make our testbed resemble the actual WFIRST CGI. Then, we will validate the WFIRST requirements by operating the testbed in the flight-like environment with a planned operational scenario.

The study in this paper is addressing the low photon flux aspect in flight. The result in Sec. 4 shows that we can generate the dark hole that meets the WFIRST raw contrast requirement using the 2nd magnitude star. The major areas of our future works include (but not limited to) (a) installing a flight-like science camera for better quantification of the science impact from the low photon flux environment, (b) inserting a flight-like OTA-S exploring the flight-like WFE, polarization effect and higher order Zernike correction, (c) installing the last remaining subsystem, Integral Field Spectrograph (IFS), for an integrated test in the OMC testbed (the IFS subsystem has been tested separately in the different testbed.), and (d) understanding the testbed drifts, which may or may not be flight relevant.

APPENDIX A. PHOTON NOISE EXPECTATION IN BATCH PROCESS

In this section, we describe how we obtain the expected values for the complex electric field uncertainty in Fig. 5. Given the probe intensities of I_k^\pm , the complex electric field, $E_R + jE_I$, is estimated using Eq. (3).

$$H \cdot \begin{pmatrix} E_R \\ E_I \end{pmatrix} = \begin{pmatrix} I_1^+ - I_1^- \\ I_2^+ - I_2^- \\ I_3^+ - I_3^- \end{pmatrix}, \quad (3)$$

where H is the ‘‘observation matrix’’ named by Groff, et.al.¹⁰ and is formulated as in Eq. (4) with the probe, P_k .

$$H = 4 \cdot \begin{pmatrix} Re\{P_1\} & Im\{P_1\} \\ Re\{P_2\} & Im\{P_2\} \\ Re\{P_3\} & Im\{P_3\} \end{pmatrix} \quad (4)$$

All variables of E , P , and I are defined in the dark hole pixel space and Eq. (3) is solved per each pixel.

We define the electric field estimation uncertainty as in Eq. (2). A simple straight-forward linear algebra leads Eq. (3) to Eq. (5).

$$\sigma^2 = \left\langle \Sigma \text{diag} \left(H^{-1} \begin{pmatrix} \sigma_1^2 & 0 & 0 \\ 0 & \sigma_2^2 & 0 \\ 0 & 0 & \sigma_3^2 \end{pmatrix} (H^{-1})^T \right) \right\rangle, \quad (5)$$

where $\langle \cdot \rangle$ denotes the spatial average in the dark hole (3-9 λ/D), Σ is for summing of the elements, $\text{diag}(\cdot)$ represents the diagonal components of the matrix, and σ_k^2 is the variance of the k 'th pair of $I_k^+ - I_k^-$.

The estimated uncertainty, marked as “x”, in Fig. 5 is based on Eq. (5). We use the empirical 4 repeated measurements for σ_k^2 as described in Sec. 3 and the estimated H for each pixel.

In a specific and ideal case when the probe amplitude are all same and the shot noise dominant, Groff, et.al., found that Eq. (5) can be simplified as,

$$\sigma^2 = \frac{1}{2n_p \cdot F_{pk} \cdot t}, \quad (6)$$

where n_p is the probe pair (3 for our case), F_{pk} is the peak intensity photon flux, and t is the single image exposure time. The other expected uncertainty, marked as solid line in Fig. 5, is based on Eq. (6) and Groff, et. al.¹⁰ called it “Noise equivalent contrast”.

ACKNOWLEDGMENTS

The research was carried out at the Jet Propulsion Laboratory, California Institute of Technology, under a contract with the National Aeronautics and Space Administration. We acknowledge X. An, D. Palmer, D. Ryan, R. Zimmer and H. Tang for their contribution to testbed layout, assembly, and alignment, J. Krist for modeling advice, F. Greer, K. Balasubramanian, V. White, and R. Calvet for device fabrication, S. Macenka, and F. Zhao for programmatic advice.

REFERENCES

1. Committee for a Decadal Survey of Astronomy and Astrophysics; Board on Physics and Astronomy; Space Studies Board; Division on Engineering and Physical Sciences; National Research Council, *New Worlds, New Horizons in Astronomy and Astrophysics*. The National Academies Press, Washington, D.C., 2010.
2. E. Cady, B.-J. Seo, B. Balasubramanian, F. Greer, B. Gordon, J. Kasdin, B. Kern, A. Kuhnert, D. Marx, C. M. Prada, D. Moody, R. Muller, I. Poberezhskiy, A. Riggs, J. Trauger, D. Wilson, V. White, K. Yee, N. Zimmerman, , and H. Zhou, “Milestone 5 Final Report: Hybrid Lyot and Shaped Pupil Broadband Contrast Testbed Demonstration for WFIRST-AFTA,” wfirst/gsf/nasa.gov/science/sdt_public/wps/references, 2015.
3. F. Shi, K. Balasubramanian, R. Bartos, R. Hein, B. Kern, J. Krist, R. Lam, D. Moore, J. Moore, K. th Patterson, I. Poberezhskiy, J. Shields, E. Sidick, H. Tang, T. Truong, K. Wallace, X. Wang, , and D. Wilson, “WFIRST Coronagraph Milestone 6 Final Report: Low Order Wavefront Sensing and Control ,” wfirst/gsf/nasa.gov/science/sdt_public/wps/references, 2015.
4. B.-J. Seo, E. Cady, B. Gordon, B. Kern, R. Lam, D. Marx, D. Moody, R. Muller, K. Patterson, I. Poberezhskiy, C. M. Prada, E. Sidick, F. Shi, J. Trauger, and D. Wilson, “Hybrid lyot coronagraph for wfirst: high-contrast broadband testbed demonstration,”
5. F. Shi, E. Cady, B.-J. Seo, X. An, K. Balasubramanian, B. Kern, R. Lam, C. M. Prada, D. Moody, K. Patterson, I. Poberezhskiy, J. Shields, H. Tang, J. Trauger, T. Truong, and D. Wilson, “Dynamic testbed demonstration of wfirst coronagraph low order wavefront sensing and control (lowfs/c),” *Proc. SPIE*, vol. 10400-13, 2017.
6. F. Shi, E. Cady, B. Kern, R. Lam, D. Marx, K. Patterson, C. M. Prada, B.-J. Seo, J. Shelton, J. Shields, H. Tang, T. Truong, and R. Zimmer, “Wfirst low order wavefront sensing and control performance under low photon flux,” *Proc. SPIE*, vol. 10698-93, 2018.
7. A. N. Cox, *Allens Astrophysical Quantities*, 4th Ed.

8. A. Give'on, B. D. Kern, and S. Shaklan, "Pair-wise, deformable mirror, image plane-based diversity electric field estimation for high contrast coronagraph," *Proc. SPIE*, vol. 8151, 2011.
9. B.-J. Seo, B. Gordon, B. Kern, A. Kuhnert, D. Moody, R. Muller, I. Poberezhskiy, J. Trauger, and D. Wilson, "Hybrid Lyot Coronagraph for WFIRST-AFTA: Occulter Fabrication and High Contrast Narrowband Testbed Demonstration," *Journal of Astronomical Telescopes, Instruments, and Systems Special Section, SPIE*, 2015.
10. T. D. Groff, A. J. E. Riggs, B. Kern, and N. J. Kasdin, "Methods and limitations of focal plane sensing, estimation, and control in high-contrast imaging," *Journal of Astronomical Telescopes, Instruments, and Systems Special Section, SPIE*, 2015.
11. L. K. Harding, R. T. Demers, M. Hoenk, P. Peddada, B. Nemati, M. Cherng, D. Michaels, L. S. Neat, A. Loc, N. Bush, D. Hall, N. Murray, J. Gow, R. Burgon, A. Holland, A. Reinheimer, P. R. Jorden, and D. Jordand, "Technology advancement of the CCD201-20 EMCCD for the WFIRST coronagraph instrument: sensor characterization and radiation damage," *Journal of Astronomical Telescopes, Instruments, and Systems Special Section, SPIE*, 2015.
12. R. J. Noll, "Zernike polynomials and atmospheric turbulence," *J. Opt. Soc. Am.*, vol. 66, p. 207, 1976.